Hydroxynaphthaldehyde Phosphate Derivatives as Potent Covalent Schiff Base Inhibitors of Fructose-1,6-bisphosphate Aldolase†

Chantal Dax,‡ Mathieu Coinçon,§ Jurgen Sygusch,§ and Casimir Blonski*,‡

Groupe de Chimie Organique Biologique, LSPCMIB UMR CNRS 5068, Université Paul Sabatier, Bâtiment IIR1, 118 Route de Narbonne, 31062 Toulouse Cedex 4, France, and Department of Biochemistry/Medicine, University of Montréal, CP 6128, Station Centre Ville, Montréal, Québec, Canada H3C 3J7

Received October 14, 2004; Revised Manuscript Received January 13, 2005

ABSTRACT: Interactions of phosphate derivatives of 2,6-dihydroxynaphthalene (NA-P_2) and 1,6-dihydroxy-2-naphthaldehyde (HNA-P, phosphate at position 6) with fructose-1,6-bisphosphate aldolase from rabbit muscle were analyzed by enzyme kinetics, difference spectroscopy, site-directed mutagenesis, mass spectrometry, and molecular dynamics. Enzyme activity was competitively inhibited by NA-P_2, whereas HNA-P exhibited slow-binding inhibition with an overall inhibition constant of ∼24 nM. HNA-P inactivation was very slowly reversed with $t_{1/2}$ ∼10 days. Mass spectrometry and spectrophotometric absorption indicated that HNA-P inactivation occurs by Schiff base formation. Rates of enzyme inactivation and Schiff base formation by HNA-P were identical and corresponded to ∼4 HNA-P molecules bound par aldolase tetramer at maximal inhibition. Site-directed mutagenesis of conserved active site lysine residues 107, 146, and 229 and Asp-33 indicated that Schiff base formation by HNA-P involved Lys-107 and was promoted by Lys-146. Titration of Lys-107 by pyridoxal 5-phosphate yielded a microscopic pK_a ∼8 for Lys-107, corroborating a role as nucleophile at pH 7.6. Site-directed mutagenesis of Ser-271, an active site residue that binds the C_1-phosphate of dihydroxyacetone phosphate, diminished HNA-P binding and enabled modeling of HNA-P in the active site. Molecular dynamics showed persistent HNA-P phosphate interactions with the C_1-phosphate binding site in the noncovalent adduct. The naphthaldehyde hydroxyl, ortho to the HNA-P aldehyde, was essential for promoting carbinolamine precursor formation by intramolecular catalysis. The simulations indicate a slow rate of enzyme inactivation due to competitive inhibition by the phenate form of HNA-P, infrequent nucleophilic attack in the phenol form, and significant conformational barrier to bond formation as well as electrostatic destabilization of protonated ketimine intermediates. Solvent accessibility by Lys-107 Nz was reduced in the covalent Schiff base complex, and in those instances where water molecules interacted with Lys-107 in the simulations, Schiff base hydrolysis was not mechanistically favorable. The findings at the molecular level corroborate the observed mechanism of slow-binding tight inhibition by HNA-P of muscle aldolase and should serve as a blueprint for future aldolase inhibitor design.

Fructose-1,6-bisphosphate aldolase (EC 4.1.2.13) is situated at the junction of the hexose and triose branches in the glycolytic pathway where it catalyzes the reversible cleavage of fructose 1,6-bisphosphate [Fru(1,6)P_2][1] to dihydroxyacetone phosphate (DHAP) and glyceraldehyde 3-phosphate (*1*, *2*). There are two distinct classes of aldolases: class I aldolases, found in eucaryotes and higher plants, are characterized by formation of a protonated imine (Schiff base) intermediate with substrates, DHAP or Fru(1,6)P_2, and the ϵ-amino group of an active site lysine residue (Lys-229) while class II aldolases, found in eubacteria and lower eucaryotes, require a divalent metal ion as a cofactor to polarize the ketose carbonyl oxygen and stabilize the enolate intermediate (*3*). The reversible aldol reaction catalyzed by class I aldolases, typified by the mammalian enzyme from rabbit muscle, proceeds by an ordered uni-bi mechanism. The multistep reaction sequence, which is supported by enzymological studies, includes formation of several distinct enzyme−substrate intermediate species. In presence of substrate, carbinolamine, imine (Schiff base), and enamine (carbanion) intermediates have been detected (*4*).

Three-dimensional crystal structures of class I aldolases have been determined from vertebrates including that of muscle (*5*−*7*), liver (*8*), insect (*9*), and parasitic protozoa (*10*, *11*). With the exception of the last 20 amino acid residues comprising the C-terminal region, the molecular architecture of these isoenzymes has been highly conserved.

† This work was supported by European Union Contract ERBIC 18CT970220 to C.B. and CIHR Grant MT-14678 (Canada) to J.S.

* Corresponding author. E-mail: blonski@cict.fr. Tel: 33 (0)5 61 55 64 86. Fax: 33 (0)5 61 55 60 11.

‡ Université Paul Sabatier.

§ University of Montréal.

[1] Abbreviations: DHAP, dihydroxyacetone phosphate; DHNA, 1,6-dihydroxy-2-naphthaldehyde; ESI, electrospray ionization; FAB, fast atom bombardment; Fru(1,6)P_2, fructose 1,6-bisphosphate; hexitol-P_2, hexitol 1,6-bisphosphate; GDH, glycerol-3-phosphate dehydrogenase; HNA-P, 1-hydroxy-2-naphthaldehyde 6-phosphate; MS, mass spectrometry; NA-P_2, naphthyl 2,6-bisphosphate; PDB, Protein Data Bank; PLP, pyridoxal 5-phosphate; PMP, pyridoxamine 5-phosphate; TEA, triethanolamine; TIM, triose-phosphate isomerase; Tris, tris(hydroxymethyl)aminomethane.

10.1021/bi0477992 CCC: $30.25
Published on Web 03/18/2005

The polypeptide fold of each 40 kDa aldolase subunit of the homotetramer corresponds to that of a β-barrel, with the active site located in the β-barrel center. The active site is composed of a substantial number of potentially charged and polar amino acid residues, which include Asp-33, Lys-107, Lys-146, Glu-187, Lys-229, and Ser-271 and which are conserved among all class I aldolases sequenced to date.

The development of active site-directed inhibitors for class I aldolases is of interest both from a mechanistic perspective (*12*−*17*) and in clinical applications. The design of pharmacologically active drugs targeting class I aldolases would be useful against microorganisms or cells where glycolysis represents the unique or primary energy source, such as in parasitic protozoa, for example, *Trypanosoma brucei*, the causative agent of African sleeping sickness (bloodstream form) (*18*, *19*), or in cancer cells (*20*). Although glycolytic aldolases have been extensively investigated, the reaction trajectory has yet to be delineated in terms of the functional roles of specific active site residues, and despite the large number of inhibitors that have been investigated none have proven particularly useful as reversible or irreversible inhibitors (*12*). Therefore, we considered the possibility of using time-dependent reversible inhibitors (slow binding) (*21*, *22*) targeting active site lysine residues (vide supra). Chemical modification (*15*, *23*−*25*) or site-directed mutagenesis (*15*, *26*) of active site lysine residues has been shown to result in the loss of enzyme activity. In a previous study (*15*), the aromatic compound 2-hydroxybenzaldehyde 4-phosphate inhibited aldolase activity by slow and reversible Schiff base formation with Lys-146 and suggested a design for novel slow-binding inhibitors of this enzyme.

In the present paper we describe the synthesis of aromatic substrate analogues of aldolase possessing a naphthyl moiety, namely, naphthyl 2,6-bisphosphate (NA-P_2) and 1-hydroxy-2-naphthaldehyde 6-phosphate (HNA-P). The mode of interaction by which the latter compound inhibits aldolase from rabbit muscle, taken as a model for class I aldolase, was determined by enzyme kinetics, UV/visible difference spectroscopy, electrospray mass spectroscopy, and site-directed mutagenesis of the active site residues. Unlike NA-P_2, which is a competitive inhibitor, time-dependent inhibition takes place in the presence of HNA-P and is concomitant with Schiff base formation between the inhibitor aldehyde and active site residue, Lys-107. Enzyme activity was only very slowly recovered upon incubation of the aldolase−inhibitor complex in a solution devoid of HNA-P. Furthermore, inhibition studies using the active site point mutant, S271A, shows that binding of the phosphate moiety of HNA-P involves the DHAP phosphate binding site. Consistency with molecular dynamics modeling studies was used to corroborate these interactions as well as examine additional interactions between HNA-P and aldolase. A mechanism for the observed slow-binding inactivation is proposed on the basis of the modeling studies.

MATERIALS AND METHODS

Materials. Fru(1,6)P_2 (sodium salt), NADH, glycerol-3-phosphate dehydrogenase (EC 1.1.1.8), and triose-phosphate isomerase (EC 5.3.1.1) were purchased from Boehringer Mannheim, dihydroxyacetone phosphate (lithium salt) was from Sigma, pyridoxamine 5-phosphate was from Fluka, and other chemicals were from Aldrich. Hexitol 1,6-bisphosphate (hexitol-P_2) was prepared from Fru(1,6)P_2 by the procedure of Ginsburg and Melher (*27*).

Scheme 1

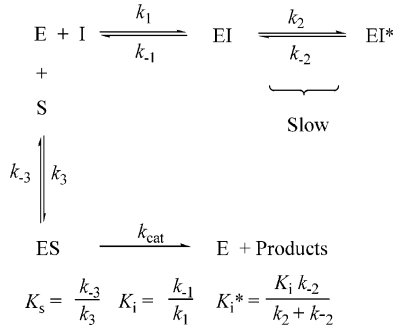

Activity Assays. Aldolase activity was measured using a coupled assay system triose-phosphate isomerase and glycerol-3-phosphate dehydrogenase (TIM/GDH) by following NADH oxidation at 340 nm using a Safas spectrophotometer thermostated to 25 °C (*28*). Assays were initiated by the addition of substrate [Fru(1,6)P_2, 1 mM final concentration] to complete a solution containing aldolase made up in triethanolamine (TEA) buffer (100 mM TEA/HCl, pH 7.6, 50 mM NaCl, 1 mM EDTA, ionic strength 0.15) and 0.42 mM NADH and containing coupling enzymes (10 μg/mL GDH and 1 μg/mL TIM) to a final volume of 1 mL. The rate of substrate cleavage was determined by measuring the decrease in absorbance per minute at 340 nm. Aldolase was dialyzed overnight at 4 °C against TEA buffer before use, and the protein concentration was determined spectrophotometrically using an extinction coefficient of $\epsilon_{280} = 0.91$ mL·mg^{-1}·cm^{-1} (*29*). The subunit concentration was determined on the basis of a molecular weight of 159000 for the aldolase tetramer (*30*).

The inhibition constant (K_i) for NA-P_2 was determined from double-reciprocal plots of initial rates measured in the presence of 10−100 μM Fru(1,6)P_2 and 0.5−1.5 μM inhibitor at constant enzyme concentration (2 μg/mL). For point mutation, K107M, assays were performed at an enzyme concentration of 30 μg/mL in the presence of 0.03−1 mM Fru(1,6)P_2 and 5−30 μM inhibitor.

Reduction by Sodium Borohydride. Sodium borohydride reduction of the aldolase−HNA-P complex (TEA buffer) was performed using a technique described previously (*15*).

Kinetic Methods. Slow-binding inhibition (*21*, *22*) involves rapid equilibrium formation between enzyme E and inhibitor I, followed by the initial complex EI undergoing a slow and reversible isomerization to a kinetically more stable complex form, EI*, as shown in Scheme 1.

For this kinetic sequence, K_i* represents the overall inhibition constant, K_i the dissociation constant for the Michaelis complex EI, and K_d the dissociation constant for the EI* complex.

(A) Characterization of Slow-Binding Inhibition. In the absence of substrate, the apparent first-order rate constant (k_{app}) describing the formation of EI* is defined by eq 1 (*31*) and exhibits saturating kinetics at increasing inhibitor concentrations ([I]) corresponding to lower and upper limits of k_{-2} and $k_2 + k_{-2}$, respectively. In the extreme situation where k_{-2} tends to zero, a slow-binding inhibitor becomes an active site-directed irreversible inhibitor.

$$k_{app} = k_{-2} + \left[k_2 \frac{[I]/K_i}{1 + [I]/K_i}\right] \quad (1)$$

$$t_{1/2} = \frac{\ln 2}{k_2}\left[1 + \frac{K_i}{[I]}\right] \quad (2)$$

At this kinetic limit, eq 1 can be rearranged to the corresponding eq 2 described by Meloche (*32*) for this type of inhibition. The half-life of enzyme inactivation ($t_{1/2}$) plotted as a function of reciprocal inhibitor concentration then represents a straight line that intercepts the ordinate at ln $2/k_2$ and the abscissa at $-1/K_i$.

Time-Dependent Reversible Inhibition Studies. Native recombinant aldolase (5 μM subunit) was incubated in the presence of HNA-P (0.05−1 mM) in TEA buffer. The enzymatic activity was assayed as a function of time with 10 μL aliquots. Inactivation kinetics followed a pseudo-first-order mechanism, and kinetic parameters K_i and k_2 were determined using eq 2.

To determine the rate of reactivation, aldolase (25 μM subunit in TEA buffer) was incubated with 500 μM HNA-P until 90% inactivation was attained. Excess inhibitor was removed by ultrafiltration using a PM-30 membrane (Millipore), and the enzyme−inhibitor complex was incubated in TEA buffer (15 μM subunit final concentration) containing hexitol-P_2 (10 mM). Aliquots (10 μL) were withdrawn at various times for determination of aldolase activity. Controls consisted of identical protocols without HNA-P. Enzyme activity monitored over 10 days period lost ∼5% of initial activity. The reactivation process was analyzed in terms of a first-order reaction.

UV/Visible Difference Spectroscopy. Absorbance spectra were measured using a Cary 1E Varian spectrophotometer at 25 °C. The same TEA buffer was used in both titration and activity assays. Absorbance spectra were measured by two different methods described elsewhere (*15*). For method A, absorption spectra were scanned either between 250 and 500 nm or at wavelengths corresponding to the maximum or minimum absorption and recorded as a function of time. Measurements were initiated by the addition of HNA-P at various final concentrations (0.1−1 mM) to TEA buffer containing a fixed concentration of aldolase (10 μM subunit). The measured absorption spectra of the enzyme complex were corrected for absorption by buffer, HNA-P, and enzyme alone. The resulting difference absorption spectra were used for determination of the rate constants describing the formation of the aldolase−HNA-P complex. Method B was used for the titration of HNA-P by aminocaproic acid. In each assay, aminocaproic acid was added at different final concentrations (0.01−0.2 M) to TEA buffer containing a fixed concentration of HNA-P (10 μM). Difference absorption spectra, corresponding to Schiff base formation, were recorded at timed intervals and corrected for absorption by buffer, aminocaproic acid, and HNA-P alone.

Apparent first-order rate constants (k_{app}) and maximal absorption differences (ΔA_{max}) were obtained for each assay by fitting the time-dependent absorption data to a first-order kinetic equation (or the sum of two first-order kinetic processes). The dissociation constant (K_d) of the Schiff base formed between HNA-P and aminocaproic acid was obtained from maximal absorption differences determined using eq 3. The dissociation constant (K_i) for the rapidly formed

$$\Delta A = \frac{\Delta A_{max}[\text{HNA-P}]}{K_d + [\text{HNA-P}]} \quad (3)$$

aldolase−HNA-P complex (EI) and rate constant k_2 corresponding to the slow formation of the EI* complex were derived from analysis of apparent first-order rate constants using eq 1 or 2.

All UV/visible difference spectroscopy experiments using aldolase mutants (10 μM subunit) were performed using method A.

Electrospray Ionization Mass Spectrometry (ESI/MS). Electrospray ionization mass spectra were obtained in the positive mode with a TSQ700 Finnigan Mat triple quadrupole mass spectrometer. Aldolase (50 μM subunits in TEA buffer) was incubated with 500 μM HNA-P until 60 ± 5% inactivation was attained, and excess inhibitor was removed by ultrafiltration using ammonium acetate buffer (10 mM, pH 5.5). The samples were prepared at ∼10 pmol/μL in H_2O/methanol (1:1 v/v) with a final concentration of 1 mM ammonium acetate and 0.5% acetic acid. Samples were infused into the source of the mass spectrometer at a continuous flow rate of 4 μL/min. Protein data were acquired over a wide scan range of m/z 500−2000 at a scan rate of 3 s per scan with a scan duration of 1 min. Spectra were transformed using the Excalibur program. The mass spectrometer was calibrated using myoglobin from horse heart (Sigma) as the standard.

Determination of Lys-107 pK_a. (A) Model Compound Titration (PMP). Pyridoxamine 5-phosphate (PMP) was used to model the adduct formed between active site Lys-107 and pyridoxal 5-phosphate (PLP) following sodium borohydride reduction (*25*). UV/visible spectra were taken at pH values ranging from 6 to 12 to confirm reported ionization potentials of the pyridine nitrogen and amino nitrogen of PMP (*33*). The pK_a's were determined from analysis of absorbance data at 325 nm that were fitted against a double pK_a equation using the program Graphit (Sigma).

(B) Labeling of Aldolase with PLP. Aldolase labeled at Lys-107 (aldolase−PMP) was prepared according to Anai et al. (*25*) except that the aldolase−PMP complex was extensively dialyzed against Tris−acetate buffer (0.1 M, pH 7.0) prior to use rather than precipitated. Residual activity of the modified aldolase was ∼30% of initial activity.

(C) Titration of Aldolase−PMP. UV/visible spectra were obtained as a function of pH (5.5−10.6) for the aldolase−PMP adduct (1 mg/mL in Tris−acetate buffer). Absorbance data of the complex were measured at 329 nm, and pK_a's were determined by the same procedure as that used for the PMP model compound. Extinction coefficient values were determined assuming an 1:1 stoichiometry of the aldolase−PMP complex.

Molecular Modeling. Molecular dynamics, using the GROMACS (*33*) package and the all-atom force field GROMOS96, was undertaken to study Michaelis and covalent complex formation with HNA-P. A high-resolution X-ray structure of tetrameric aldolase wherein DHAP was noncovalently bound in the active site (*6*) was used as template for inhibitor modeling.

In noncovalent forms of the complex, the HNA-P molecule was manually docked in the active site cleft by first

superimposing its phosphate moiety onto the phosphate binding site (binding mode A) in a manner that preserves the same hydrogen-bonding pattern including the oxyanion interaction with Ser-271. The HNA-P aldehyde function was then aligned such that it would be capable of hydrogen bonding with Lys-107 by adjusting torsion angles about the P−O ester bond, ω_1, and the ester oxygen C_6 carbon bond, ω_2. Hydrogen bonding by the oxygen aldehyde with Lys-107 resulted simultaneously in contacts between C_1−OH and Lys-146 as well as Asp-33.

To explore conformations suitable for Schiff base formation with Lys-107, simulations were conducted using the nucleophilic form of Lys-107. The naphthyl C_1−OH has a pK_a of 8.0 (*34*), such that at pH 7.6 used for inactivation, both phenol and phenate forms are present in sufficient concentrations, and simulations were performed wherein each phenolic species was used. Asp-109 OD2 was protonated to mimic proton transfer from Lys-107 and to reduce electrostatic interaction with the C_{11} carbonyl oxygen of the aldehyde moiety. The C_{11} carbonyl was chosen oriented cis with respect to the C_1−O_1 bond in the phenol form, maximizing its hydrogen-bonding interaction with the O_1 hydroxyl. In case of the phenate form, the C_{11} carbonyl was oriented trans with respect to C_1−O_1 bond to minimize repulsion with the O_1 hydroxyl ion. These two orientations represented all conformations found for *o*-hydroxybenzaldehyde molecular fragments in the Cambridge Structural Database.

Covalent complexes were modeled as protonated imines having the Lys-107 Nz atom covalently bound to the C_{11} atom of HNA-P. Steric clashes narrowed the model building of the HNA-P covalent complex to a conformation wherein HNA-P occluded the active site, allowing the phosphate oxyanion to potentially interact with Ser-38 as well as the charge cluster formed by Lys-41, Arg-42, and Arg-303.

The force field parameters for HNA-P were chosen on the basis of similar chemical moieties parametrized in the GROMOS96 force field (parameter set 43a1). All constructs were immersed in a dodecahedron box filled with SPC (simple point charge) water molecules imposing a minimum solute-wall box of 10 Å surrounding the aldolase subunit.

Simulations were performed with periodic boundary conditions at constant *T* (300 K) and *p* (1 bar) using the Berendsen method (*33*) with a coupling constant of 0.1 ps for temperature and 0.5 ps for pressure. The time step for dynamics was 2 fs using the LINCS algorithm (*34*). A twin-range cutoff method was used for nonbonded interactions. The electrostatic interactions were calculated by the particle mesh Ewald (*35*) method with a 9 Å cutoff for electrostatic interactions and the Lennard-Jones interactions with a 14 Å cutoff. The pair list of atoms interacting together was updated every five steps and kept constant between updates.

Close contacts in the initial model, if any, were relieved by 600 cycles of steepest descent energy minimization and an additional 1000 cycles of conjugated gradient energy minimization. Minimizations were followed by a 20 ps molecular dynamics with positional restraints on protein non-hydrogen atoms to relax water molecules around the subunit; this was followed by an additional 200 ps of molecular dynamics without restraints to allow for system equilibration. The protocol yielded RMS values for energy derivatives as a function of the C_α position that were less than 1.8 Å with respect to the crystallographic coordinates of the subunit.

Simulations of 5 ns duration were conducted for each modeled structure. Atomic coordinates generated by the dynamical simulations were sampled at a frequency of 1 ps. The atomic coordinate frames and corresponding potential energies were then used to calculate appropriate model conformational statistics. A unit-weighting scheme was employed for calculation of time averages and corresponding standard deviations. Standard deviations are reported using the symbol ±. The larger the standard deviation, compared to the statistical average, the greater the configurational heterogeneity.

Geometry conducive for incipient formation of the carbinolamine precursor was used to filter configurations generated in the simulations. Candidate geometry competent for attack was analyzed whenever the attacking nucleophile, Lys-107 Nz atom, was less than the van der Waals distance from the electrophilic aldehyde C_{11} carbon. The angle of attack was calculated as the direction defined by the Lys-107 Nz atom and C_{11} carbon and the normal to the hybridization plane containing the aldehyde C_{11} carbon.

Aldolases. Expression and purification of recombinant rabbit muscle aldolases were as reported previously (*36*, *37*). Purification was based on substrate affinity elution from the carboxymethyl-Sepharose stationary phase and using gel filtration for protein cleanup.

Chemical Syntheses. The NMR spectra were recorded in $CDCl_3$, CD_3OD, or D_2O with a Bruker AC200 (200 MHz ^{1}H NMR, 50 MHz ^{13}C NMR, and 81 MHz ^{31}P NMR), a Bruker AC250 (250 MHz ^{1}H NMR, 62 MHz ^{13}C NMR), or a Bruker ARX400 (400 MHz ^{1}H NMR, 100 MHz ^{13}C NMR) spectrometer. All chemical shifts are reported in parts per million with respect to TMS for ^{1}H and ^{13}C NMR spectra and H_3PO_4 for ^{31}P NMR spectra as internal standards. Naphthyl 2,6-bisphosphate (NA-P_2) was prepared as described previously (*38*) and HNA-P according to Scheme 2.

*(A) 2-[(Z)-1-Hydroxymethylidene]-6-methoxy-1,2,3,4-tetrahydro-1-naphthalenone (**1**).* To a mixture of sodium methoxide (11.1 g, 205.6 mmol) and ethyl formate (9 mL, 111.4 mmol) in dry benzene (70 mL) at room temperature was added dropwise a solution of 6-methoxy-1-tetralone (8.4 g, 47.6 mmol) in dry benzene (40 mL). After addition, the reaction mixture was stirred at room temperature for 4 h. Et_2O (50 mL) was added, and the resulting mixture was washed with water, pH = 12. The pH of the aqueous layer was adjusted to 4 and extracted with Et_2O. The organic layer was washed with water and brine, then dried over $MgSO_4$, and evaporated under reduced pressure to yield **1** as a brownish powder (9.22 g, 95%). ^{1}H NMR (250 MHz, $CDCl_3$): δ 2.54 (m, 2H, H3), 2.86 (m, 2H, H4), 3.94 (s, 3H, OCH_3), 6.61 (d, $^4J_{H5-H7}$ = 2.50 Hz, 1H, H5), 6.82 (dd, $^4J_{H5-H7}$ = 2.50 Hz, $^3J_{H7-H8}$ = 8.50 Hz, 1H, H7), 7.92 (d, $^3J_{H8-H7}$ = 8.50 Hz, 1H, CH8), 9.88 (s, 1H, CH), 12.28 (br, 1H, OH). ^{13}C NMR (62 MHz, $CDCl_3$): δ 23.3 (C4), 29.37 (C3), 55.51 (OCH_3), 108.21 (C_2), 112.67 (C5), 113.05 (C7), 126.22 (C10), 128.82 (C8), 144.49 (C9), 163.4 (C6), 175.12 (CHOH), 208.07 (C1). Mass spectrometry (DCI/NH_3): 204 ($M + H^+$, 100%), 222 ($M + NH_4^+$, 15%).

*(B) 1-Hydroxy-6-methoxy-2-naphthaldehyde (**2**).* A mixture of naphthalenone (**1**) (4.2 g, 20.74 mmol) and dichloro-2,3-dicyano-5,6-benzoquinone (5.20 g, 22.92 mmol) in dioxane

Scheme 2: Synthetic Scheme for the Synthesis of HNA-P (**5**)[a]

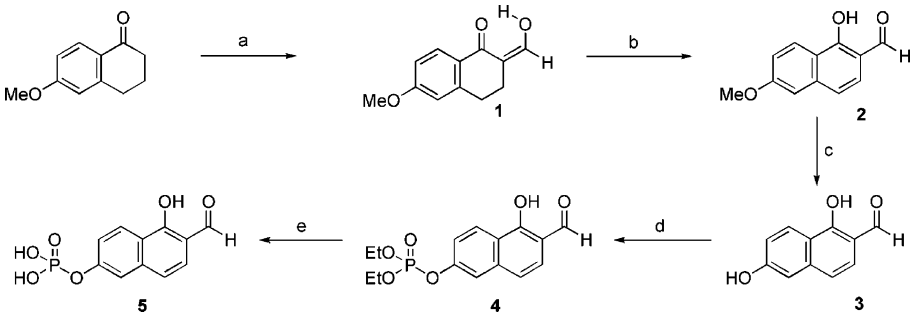

[a] Conditions: (a) MeONa, ethyl formate, benzene, room temperature; (b) DDQ, dioxane, room temperature; (c) BBr_3, CH_2Cl_2, −40 °C; (d) $(EtO)_3P$, pyridine, I_2, CH_2Cl_2 ; (e) Me_3SiBr, CH_2Cl_2, room temperature, H_2O.

(90 mL) was stirred at room temperature for 1 h. The hydroquinone was filtered off, and the solvent was removed under reduced pressure. The remaining product was purified by flash chromatography (CH_2Cl_2) to yield **2** as an yellow powder (4.1 g, 98%). ^{1}H NMR (200 MHz, $CDCl_3$): δ 3.91 (s, 3H, OCH_3), 7.01 (d, $^4J_{H5-H7}$ = 2 Hz, 1H, H5), 7.13 (dd, $^3J_{H5-H7}$ = 2 Hz, $^3J_{H7-H8}$ = 7.3 Hz, 1H, H7), 7.17 (d, $^3J_{H8-H7}$ = 7.3 Hz, 1H, H8), 7.36 (d, $^3J_{H3-H4}$ = 7.3 Hz, 1H, H3), 9.84 (s, 1H, CHO), 12.67 (s, 1H, OH). ^{13}C NMR (50 MHz, $CDCl_3$): δ 55.44 (OCH_3), 106.34 (C4), 113.28 (C2), 116.23 (C3), 116.43 (C8), 119.04 (C10), 126.12 (C5), 127.51 (C7), 139.62 (C9), 161.55 (C6), 162.03 (C1), 195.62 (CHO). Mass spectrometry (DCI/NH_3): 203 (M + H^+, 100%), 220 (M + NH_4^+, 17%).

*(C) 1,6-Dihydroxy-2-naphthaldehyde (**3**) (DHNA).* A 1.0 M solution of boron tribromide in CH_2Cl_2 (15 mL, 15 mmol) was added dropwise to a stirred solution of compound **2** (0.577 g, 2.85 mmol) in dry CH_2Cl_2 (120 mL) at −40 °C. The resulting mixture was stirred additionally for 1 h at −40 °C and then allowed to warm to room temperature. Water (20 mL) was added. The organic layer was washed by water (20 mL) and brine (20 mL) and dried over $MgSO_4$, and the solvent was evaporated under reduced pressure. The crude residue was purified by flash chromatography (CH_2Cl_2 to CH_2Cl_2/Et_2O, 1:1) to yield **3** as an orange powder (0.314 g, 59%).^{1}H NMR (400 MHz, CD_3OD): δ 7.03 (d, $^4J_{H5-H7}$ = 2.37 Hz, 1H, H5), 7.07 (dd, $^4J_{H5-H7}$ = 2.40 Hz, $^3J_{H7-H8}$ = 9 Hz, 1H, H7), 7.13 (d, $^3J_{H4-H3}$ = 8.49 Hz, 1H, H4), 7.40 (d, $^3J_{H4-H3}$ = 8.50 Hz, 1H, H3), 8.21 (dd, $^3J_{H8-H7}$ = 9 Hz, $^4J_{H8-H5}$ = 0.50 Hz, 1H, H8), 9.91 (s, 1H, CHO). ^{13}C NMR (100 MHz, CD_3OD): δ 110.65 (CH5), 114.23 (C2), 119.06 (CH7), 119.23 (CH4), 119.40 (C9), 127.18 (CH8), 128.48 (CH3), 141.68 (C10), 161.28 (C6), 163.05 (C1), 197.44 (CHO). Mass spectrometry (DCI/NH_3): 189 (M + H^+, 100%), 206 (M + NH_4^+, 32%).

*(D) 1-Hydroxy-2-naphthaldehyde 6-Diethyl Phosphate (**4**).* To a solution of compound **3** (0.21 g, 1.1 mmol) in CH_2Cl_2 (34 mL) was added dry pyridine (0.1 mL, 1.24 mmol) at 0 °C, followed by the addition of a mixture of iodine (0.31 g, 1.2 mmol) and triethyl phosphite (0.23 mL, 1.32 mmol) in CH_2Cl_2 (10 mL). The resulting mixture was stirred for 1 h at 0 °C and allowed to warm to room temperature. Water (20 mL) was added, the organic layer was washed by brine and dried over $MgSO_4$, and the solvent was removed under reduced pressure. The remaining product after flash chromatography (CH_2Cl_2) yielded compound **4** as a yellow oil (0.11 g, 31%). ^{1}H NMR (200 MHz, $CDCl_3$): δ 1.34 (t, $^3J_{H-H}$ = 7 Hz, 6H, CH3), 4.24 (q, $^3J_{H-H}$ = 7 Hz, 4H, CH2), 7.26 (d, $^3J_{H3-H4}$ = 8.59 Hz, 1H, H3), 7.35 (dd, $^4J_{H7-H5}$ = 2.27 Hz, $^3J_{H7-H8}$ = 9.10 Hz, 1H, H7), 7.44 (d, $^3J_{H4-H3}$ = 8.59 Hz, 1H, H4), 7.59 (se, 1H, H5), 8.37 (d, $^3J_{H8-H7}$ = 9.10 Hz, 1H, H8), 9.91 (s, 1H, CHO). ^{13}C NMR (50 MHz, $CDCl_3$): δ 16.11 (d, $^3J_{C-P}$ = 6.40 Hz, CH3), 64.9 (d, $^2J_{C-P}$ = 6.10 Hz, CH2), 114.11 (C10), 116.36 (d, $^3J_{C-P}$ = 4.70 Hz, C5), 118.99 (C3), 119.90 (d, $^3J_{C-P}$ = 5.70 Hz, C7), 126.75 (C4), 127.69 (C8), 138.83 (C2), 152.27 (d, $^2J_{C-P}$ = 6.95 Hz, C6), 161.70 (C1), 196.10 (CHO). ^{31}P NMR (81 MHz, $CDCl_3$): δ −6.80. Mass spectrometry (DCI/NH_3): 325 (M + H^+, 56%), 342 (M + NH_4^+, 100%).

*(E) 1-Hydroxy-2-naphthaldehyde 6-Phosphate (Sodium Salt) (**5**) (HNA-P).* Bromotrimethylsilane (0.15 mL, 1.1 mmol) was added slowly with stirring to a solution of protected phosphate **4** (0.054 g, 0.17 mmol) in dry CH_2Cl_2 (200 μL) under nitrogen atmosphere. The resulting mixture was stirred for 3 h at room temperature (the progress of the reaction was monitored by ^{31}P NMR). Then Et_2O/H_2O (10:1) was added, and the organic layer was washed by water (10 mL). The pH of the aqueous layer was adjusted to 7.6 with aqueous NaOH (1 M); the solution was freeze-dried to yield **5** as a white powder (0.050 g, 96%). ^{1}H NMR (250 MHz, D_2O): δ 7.11 (d, $^3J_{H3-H4}$ = 8.50 Hz, 1H, H3), 7.34 (d, $^3J_{H7-H8}$ = 8.00 Hz, 1H, H7), 7.41 (se, 1H, H5), 8.24 (d, $^3J_{H4-H3}$ = 8.50 Hz, 1H, H4), 9.84 (d, $^3J_{H8-H7}$ = 8.00 Hz, 1H, H8), 9.91 (s, 1H, CHO). ^{13}C NMR (50 MHz, D_2O): δ 114.73 (C2), 116.93 (C10), 118.32 (d, $^3J_{C-P}$ = 3.57 Hz, C5), 120.13 (C8), 123.36 (d, $^3J_{C-P}$ = 5.00 Hz, C7), 123.42 (C9), 126.72 (C3), 128.31 (C4), 142.35 (C1), 158.49 (d, $^2J_{C-P}$ = 6.00 Hz, C6), 198.32 (CHO). ^{31}P NMR (81 MHz, D2O): δ 0.56. Mass spectrometry (FAB$^-$): 267. $\lambda_{max}^{H_2O}$ (pH 7.6): 392 nm (ϵ 5100 $M^{-1}\cdot cm^{-1}$), 277 nm (ϵ 4650 $M^{-1}\cdot cm^{-1}$).

RESULTS

Competitive Inhibition of Rabbit Muscle Aldolase by NA-P_2. The Fru(1,6)P_2 analogue, NA-P_2, competitively inhibited the aldolase-catalyzed reaction consistent with an inhibition constant, K_i, of 0.28 ± 0.03 μM. The Michaelis constant (K_m) determined for Fru(1,6)P_2 as substrate was 13 ± 2 μM. Both K_i and K_m values increased to 13 ± 1 μM and 150 ± 15 μM, respectively, when the assays were performed with the K107M mutant. From differential protection experiments, Lys-107 has been shown to interact with the C_6 phosphate of Fru(1,6)P_2 (*25*). The decreased affinity, with respect to the wild-type enzyme for both inhibitor and substrate, by the point mutation Lys-107 to Met suggests that Lys-107 also interacts with a phosphate moiety on NA-P_2.

Table 1: Interaction of HNA-P with Aldolase

conditions[a]	specific acitvity (units/mg)[b]
enzyme alone	12.5 ± 0.5
enzyme + HNA-P	2.8 ± 0.3
enzyme + HNA-P + Fru(1,6)P_2	5.2 ± 0.4
enzyme + HNA-P + hexitol-P_2	9.9 ± 0.5
enzyme + DHNA	12.5 ± 0.5

[a] Native rabbit muscle aldolase (0.2 mg/mL) was incubated in the presence of a fixed concentration of HNA-P (250 μM) in TEA buffer (1 mL final volume, pH 7.6) with or without Fru(1,2)P_2 or hexitol-P_2 (1 mM). [b] Aliquots were analyzed after 80 min incubation time for enzymatic activity (see the Materials and Methods section). In control experiments performed with enzyme alone or in the presence of DHNA (250 μM), no loss of enzyme activity was detected.

Table 2: Kinetic Parameters Describing the Interaction of HNA-P with Aldolase in TEA Buffer (pH 7.6)

parameter	value
K_i (μM)	125 ± 25[a]
k_2 (min^{-1})	0.067 ± 0.03[a]
k_{-2} (min^{-1})	$(13 \pm 3) \times 10^{-6}$ [b]
K_i* (nM)	24 ± 5

[a] Calculated using eq 3. [b] Calculated from data corresponding to enzymatic activity recovered (see the Materials and Methods section).

Time-Dependent Reversible Inhibition of Aldolase by HNA-P. Incubation of aldolase with HNA-P leads to a first-order loss of enzyme activity (kinetics not shown). Substrate Fru(1,6)P_2 and substrate analogue hexitol-P_2, a strong competitive inhibitor for the aldolase-catalyzed reaction (*27*), protected the enzyme against inactivation by HNA-P (Table 1), consistent with inactivation occurring at the active site. By contrast, under identical experimental conditions, described in Table 1, the nonphosphorylated hydroxynaphthaldehyde DHNA analogue (see Scheme 2) was completely inactive against aldolase, indicating a functional role for the phosphate group in mediating active site binding by HNA-P. The aldolase inactivation rate was saturating with respect to increasing HNA-P concentrations and was analyzed as an irreversible process (Scheme 1 with $k_{-2} = 0$). Kinetic parameters were derived from the apparent first-order rate constant (k_{app}) measured at different inhibitor concentrations (0.01−1.5 mM) according to eq 2 and are shown in Table 2.

Enzyme activity, representing $20 \pm 5\%$ of the initial value, was recovered after 10 days incubation of the inactivated enzyme in a solution devoid of HNA-P and containing a saturating concentration of hexitol-P_2. Recovery of enzyme activity, analyzed as a first-order process, furnished the microscopic rate constant [$k_{-2} = (1.3 \pm 0.3) \times 10^{-5}$ min^{-1}]. The recovery of enzymatic activity is 4 orders of magnitude smaller than the inactivation constant k_2, consistent with determination of k_2 using the kinetic approximation of irreversible inactivation. HNA-P, therefore, behaves as a slow-binding inhibitor, and from the values shown in Table 2, the overall dissociation constant K_i* was calculated to be 24 ± 5 nM. Moreover, enzyme activity could not be restored after treatment of the enzyme−inhibitor complex with sodium borohydride, suggesting that the mechanism of inhibition by HNA-P involves Schiff base formation with an active site lysine residue.

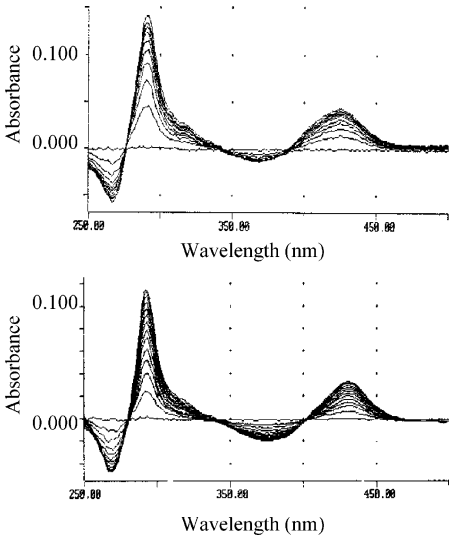

FIGURE 1: Interaction of HNA-P with aminocaproic acid and with native recombinant rabbit muscle aldolase. Upper panel: UV/visible difference spectra of a mixture of 10 μM HNA-P and 200 mM aminocaproic acid in TEA buffer (1 mL, pH 7.6) with time (10 min intervals). Lower panel: UV/visible difference spectra of aldolase (10 μM subunits) and 250 μM HNA-P in the same buffer with time (interval of 5 min).

Interaction of HNA-P with Aminocaproic Acid. Schiff base formation between HNA-P and the ϵ-amino group of aldolase lysine residues was modeled using the reaction of HNA-P (10 μM) with aminocaproic acid (0.1−1 mM) as reference and was monitored by UV/visible difference spectroscopy (*15*). Schiff base formation between amino acids and aromatic hydroxyaldehydes such as pyridoxal or salicylaldehyde can be followed by difference spectroscopy and has been reported previously (*39*−*41*). The model reaction, shown in Figure 1 (upper panel), is characterized by changes in UV/visible absorbencies that correspond to two maxima at 425 nm ($\Delta\epsilon$ 3730 ± 200 $M^{-1}\cdot cm^{-1}$) and 291 nm ($\Delta\epsilon$ 13080 ± 700 $M^{-1}\cdot cm^{-1}$), which can be ascribed to Schiff base formation, and two minima at 367 nm ($\Delta\epsilon$ −740 ± 50 $M^{-1}\cdot cm^{-1}$) and 267 nm ($\Delta\epsilon$ −5050 ± 300 $M^{-1}\cdot cm^{-1}$) resulting from HNA-P consumption due to covalent complex formation. The presence of isosbestic points at 388, 343, and 276 nm indicates an absence of side reactions and no intermediate accumulation. Differential absorbance changes at equilibrium were found to be saturating with increasing aminocaproic acid concentrations (see Figure 2), and reaction kinetics for each aminocaproic acid concentration were consistent with a pseudo-first-order rate process for the reaction and corresponding to a second-order rate constant, k_{2nd}, of 0.12 ± 0.01 $M^{-1}\cdot min^{-1}$ at 25 °C. The value of the dissociation constant, K_d, for the HNA-P−aminocaproic acid adduct was 16 ± 3 mM (see Figure 2).

Interaction between HNA-P and Aldolase. When HNA-P (0.1−1 mM, final concentration) was added to a solution containing native aldolase (10 μM subunits), the resulting UV/visible difference spectra have maxima at 431 and 293 nm and minima at 376 and 268 nm, with isosbestic points at 401 and 279 nm (Figure 1, lower panel). Slight differences in band positions with respect to the model reaction can be attributed to differences in the protein environment of HNA-P with respect to the model system and have been observed in other studies (*15*, *39*). The progress of absorbance difference

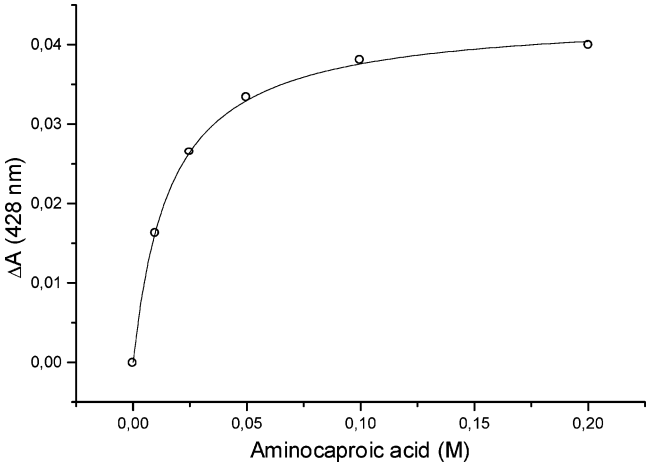

FIGURE 2: Change in differential absorbance as a function of aminocaproic acid concentration. Differential absorbance at equilibrium was measured at 425 nm in TEA buffer (pH 7.6). The concentration of HNA-P was 10 μM. Data points are experimental, and the line represents the best fit of the data to eq 3. The K_d value determined was 16 ± 3 mM.

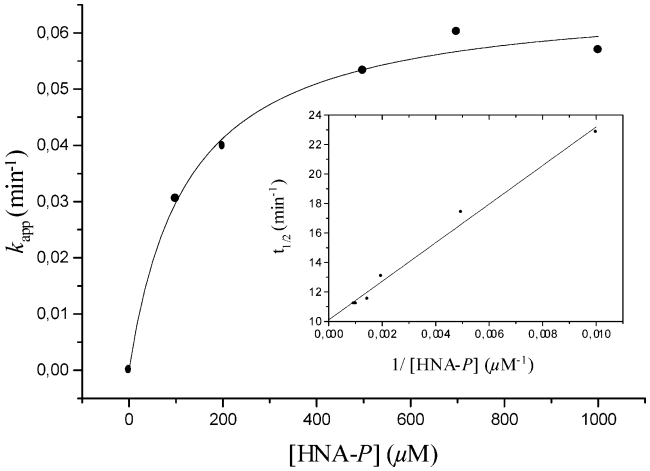

FIGURE 3: Saturation kinetics of the Schiff base formation between native recombinant rabbit muscle aldolase and HNA-P. Shown is the variation of apparent first-order rate constant of Schiff base formation (k_{app}) between aldolase (10 μM subunits) and HNA-P at various concentrations in TEA buffer (pH 7.6). The line shown was derived from nonlinear regression of experimental data (symbols) analyzed according to eq 1. In the insert is shown the linear regression of the experimental data ($t_{1/2}$) analyzed according to eq 2. The best fit corresponded to values of K_i = 125 ± 25 μM and k_2 = 0.067 ± 0.003 min^{-1}.

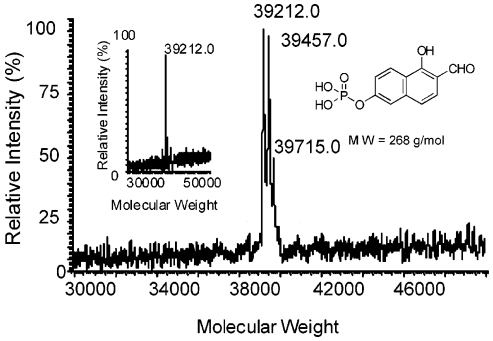

FIGURE 4: Deconvoluted electrospray ionization mass spectrum of the aldolase−HNA-P complex (40% residual activity). Samples were prepared at ~10 pmol/μL in 50% MeOH, 50% H_2O, 1 mM ammonium acetate, and 0.5% acetic acid and were infused at 4 μL/min. Several scans (~20) from *m*/*z* 500 to *m*/*z* 2000 at a scan rate of 3 s per scan were summed to yield the final profile spectrum prior to deconvolution. In the insert is shown the deconvoluted electrospray ionization mass spectrum of native recombinant aldolase prior to inhibition.

spectra was consistent with two distinct first-order rate processes. The rapid kinetic phase displayed the larger absorbance change and saturating behavior at high inhibitor concentrations and correlated with complete loss of enzyme activity and was made use of in the subsequent analyses. A slow kinetic phase was also observed when the assays were run in the presence of a saturating concentration of the protective substrate analogue hexitol-P_2 (10 mM). This slow kinetic phase, which corresponds to a 30 times smaller rate constant and contributes one-fourth of the final absorbance change, is not related to the observed inhibition and was not further analyzed. The same absorbance change at equilibrium (for the rapid kinetic phase) was observed over the entire range of inhibitor concentrations used. At these saturating concentrations, molar absorption coefficients for bound HNA-P were calculated by assuming that all four active sites of aldolase were occupied and yielded $\Delta\epsilon_{431}$ = 3600 ± 200 M^{-1}·cm^{-1}, $\Delta\epsilon_{376}$ = −2140 ± 110 M^{-1}·cm^{-1}, $\Delta\epsilon_{293}$ = 12480 ± 650 M^{-1}·cm^{-1}, and $\Delta\epsilon_{268}$ = −5080 ± 250 M^{-1}·cm^{-1}. The resulting stoichiometry of HNA-P bound to aldolase at maximal inhibition is consistent with differential molecular absorbencies derived from the aminocaproic acid−HNA-P complex given above, which predict an EI* complex having 3.9−4.2 mol of HNA-P bound/mol of tetrameric aldolase.

Kinetic parameters, K_i and k_2, describing EI* complex formation, were determined from data shown in Figure 3 according to eq 1 or 2 and yielded values of K_i = 125 ± 25 μM and k_2 = 0.067 ± 0.004 min^{-1}, which are in good agreement with those determined kinetically (Table 2). The overall dissociation constant K_i* calculated from these results corresponds to 24 ± 5 nM. Thus, the reactivity of HNA-P toward aldolase, as defined by (k_2/K_i), is about 4000-fold enhanced with respect to the reaction with model compound aminocaproic acid (k_{2nd}). Moreover, the dissociation constant of the HNA-P−aminocaproic acid complex is about 4 × 10^5-fold weaker than that of the aldolase−HNA-P complex. Thus, the aldolase active site contributes about 7.5 kcal mol^{-1} of binding energy to the Schiff base complex.

ESI/MS Analysis of the Aldolase−HNA-P Complex. ESI analysis of an aldolase−HNA-P complex yielded molecular masses corresponding to a free aldolase monomer (39212 Da), a binary complex between an aldolase subunit and HNA-P (39457 Da), and a minor species consisting of a ternary complex between an aldolase subunit and two HNA-P molecules (39715 Da) (Figure 4). Observation of binary and ternary complexes is consistent with molecular masses that correspond to Schiff base complexes between an aldolase subunit and inhibitor at the expected stoichiometries of 1:1 and 1:2, respectively. The presence of both free and modified enzyme is compatible with UV/visible kinetic data and agrees with an observed 60% loss in initial activity.

Interaction between Aldolase Mutants and HNA-P. (A) Lysine Mutants. Lysine residues 107, 146, and 229 are located in the aldolase active site and thus are candidates for mediating inactivation through Schiff base formation with HNA-P. To identify which lysine residue was responsible for the differential absorbencies observed in the presence of

Table 3: Interaction of HNA-P with Recombinant Mutant Aldolases[a]

aldolase	specific acitivity (units/mg)	residual specific activity (%)	analysis of k_{app} (min^{-1})	relative ΔA of resolved species at 431 nm (%)
native	12.5	nd	0.045(3)[b]	100[c]
			0.0015(3)	*25*
K229M	3×10^{-6}	nd	0.040(3)[b]	95[c]
			0.0015(3)	*25*
K146M	2×10^{-3}	nd	0.0050(5)[b]	98[c]
			0.0015(3)	*25*
K107M	0.7	95	0.0015(3)	30
D33S	2×10^{-3}	nd	0.0070(5)	97
D33N	3×10^{-3}	nd	0.023(2)	98

[a] Assays were performed in TEA buffer (pH 7.6) according to method A (see the Materials and Methods section) at fixed aldolase subunit concentrations (10 μM subunits) and HNA-P concentrations (300 μM). Rates of Schiff base formation were monitored at 431 nm and could be analyzed by two first-order processes. For these cases, the rapid phase displaying the larger absorbance change is correlated with the loss of enzyme activity. The results obtained for the slow process are indicated in italics. nd = not detectable. [b] Standard deviation given in parentheses and corresponds to last significant figure for each rate constant. [c] Relative amplitude for rapid phase.

HNA-P, point mutations of these lysine residues were constructed, namely, K107M, K146M, and K229M. These active site mutants possess no charge, are isosteric, and are unable to participate in Schiff base formation. Comparison of atomic coordinates for K107M, K229M, and native enzyme[2] shows these mutant structures to be isomorphous with respect to wild-type enzyme (RMS deviations of atomic coordinates with respect to native aldolase are 0.41 and 0.48 Å for K107M and K229M structures, respectively). UV/visible difference spectroscopy (method A) was used to examine the formation of the enzymatic complex for each point mutation in the presence of a fixed HNA-P concentration (300 μM), and analysis of the resulting data at 431 nm is reported in Table 3.

Difference spectra observed for the mutant K229M were identical to that observed with wild-type enzyme. The progress of the reaction could be accounted for by two distinct first-order processes. The kinetic parameters and the amount of EI* complex formed were identical with those of the wild-type enzyme and rule out Lys-229 as the lysine residue directly responsible for Schiff base formation.

In contrast, difference spectra of the K107M mutant plus HNA-P showed only a slow kinetic phase whose rate constant and maximal absorbance were identical to the values of the slow phase observed for the wild-type enzyme. The absence of a rapid phase together with the absence of enzyme inhibition is consistent with Lys-107 being responsible for the observed slow-binding inhibition.

Reaction of the K146M mutant with HNA-P resulted in an overall absorbance change at an equilibrium comparable with that observed for wild-type aldolase (Table 3). The kinetic phase associated with enzyme inhibition, although corresponding to a first-order rate process, differed from that observed in the wild-type enzyme, exhibiting very slow Schiff base formation. The substitution of Lys-146 with Met thus results in a decrease in the rate of EI* complex formation, but it does not change the ability by the mutant to form the complex. Thus, Lys-146 is not required for Schiff base formation but merely facilitates it.

Similarly, reaction by D33N and D33S mutants resulted in an overall absorbance change at equilibrium similar to that of the wild-type aldolase (Table 3). The kinetic phase associated with enzyme inhibition corresponded to a first-order rate process and was consistent with diminished Schiff base formation. Different from other mutants, the very slow rate process was not observed, indicating that loss of the carboxylate moiety suppresses the HNA-P side reaction and implying that the side reaction depends on the integrity of the C_6-phosphate binding locus. The same carboxylate oxygen of Asp-33 interacts with both Lys-107 and Lys-146 in the active site of the native enzyme such that loss of Asp-33 negative charge as well as its interaction with the lysine residues in the point mutant D33S may destabilize Lys-107 and Lys-146 side chain conformations. Both Lys-107 and Lys-146 are responsible for promoting substrate C_6-phosphate binding in aldolases (*24*).

(B) Ser-271 Mutant. The phosphate moiety of HNA-P is essential for aldolase interaction as the analogue DHNA, which lacks the phosphate moiety, is only a very weak inhibitor (Table 1). DHAP binding in rabbit muscle aldolase places the phosphate moiety of the reactant within hydrogen-bonding distance of Ser-271 (*6*), suggesting that this residue may participate in the binding and positioning of HNA-P in the active site. To examine this hypothesis, the active site mutant S271A, which is unable to participate in hydrogen bonding with the phosphate oxyanion, was employed.

The mutant S271A exhibited considerably lowered activity and affinity toward Fru(1,6)P_2 (specific activity = 0.05 unit/mg and K_m = 1 mM), indicating a functional role for Ser-271 in catalysis. UV/visible difference spectra of the S271A mutant (10 μM subunits) in the presence of HNA-P (0.1−1.5 mM) were consistent with two distinct first-order kinetic processes, identical with those observed in the wild-type enzyme (see Figure 1). The stoichiometry of HNA-P binding to the S271A mutant corresponds under saturating conditions to an EI* complex wherein ~4 mol of inhibitor is bound per mole of tetrameric mutant aldolase. Kinetic analysis of data corresponding to EI* complex formation yielded values for K_i and k_2 of 1.3 ± 0.1 mM and 0.065 ± 0.006 min^{-1}, respectively. Thus, the mutation Ser-271 to Ala decreases by 1 order of magnitude the affinity of HNA-P for the aldolase active site but did not modify its ability to catalyze Schiff base formation. The contribution of the hydroxyl moiety of Ser-271 to binding energy of the HNA-P phosphate moiety in the aldolase-HNA-P complex is thus ~1.4 kcal·mol^{-1}.

Ionization Constant of the Amino Group of Lys-107. PLP reacts covalently with muscle aldolase by Schiff base formation with Lys-107, which inhibits enzymatic activity (*25*). The resulting complex can be reduced in the presence of sodium borohydride ions, resulting in PMP becoming irreversibly bound to the ϵ-amino group of Lys-107. Bound PMP is spectrophotometrically detectable and thus useful as a "reporter group" (*42*) at the active site of the enzyme. By comparison of pK_a's of the substituted pyridine nitrogen and ammonium ion of the reporter group with those of unbound

[2] Atomic coordinates for the DHAP native complex and mutants K107M and K229M are available from the Research Collaboratory for Structural Bioinformatics Protein Databank (http://www.rcsb.org/pdb/) deposited under accession codes 1ADO, 1EWD, and 1EWE, respectively.

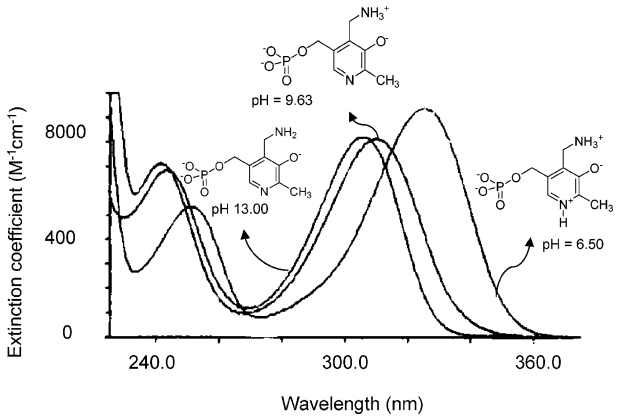

FIGURE 5: Absorption spectra of pyridoxamine 5-phosphate taken at pH 6.50, 9.63, and 13.0. At the pH shown, the observed spectra arise predominantly from the indicated species.

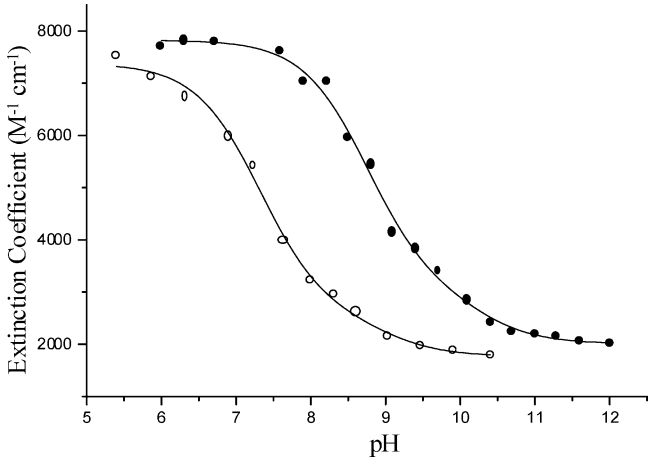

FIGURE 6: Absorption spectra of PMP at 325 nm (solid circles) and the PMP−aldolase complex at 329 nm (open circles) as a function of pH. The best fit using the Graphit program (double pK_a equation) corresponded to pK_a values of 8.75 ± 0.08 and 10.5 ± 0.4 for PMP and 6.9 ± 0.1 and 8.3 ± 0.5 for the PMP−aldolase complex.

PMP, the perturbation of the active site environment on the ionization potential can be estimated. The pK_a of the substituted phenol (pK_a ~3.7) was not used in this study due to poor stability of the enzyme at low pH.

(A) Model Compound. UV/visible spectra of PMP at pH 6.50, 9.63, and 13.0 are shown in Figure 5, and each absorption spectrum illustrated corresponds to the predominant species present at the given pH (*43*). Substantial spectral changes accompany titration of the substituted pyridinium ion (λ_{max} 325 nm) to the corresponding pyridine (λ_{max} 309 nm) while only a small but measurable spectral shift occurs upon neutralization of the ammonium salt group (λ_{max} 305 nm). The change in absorbance at 325 nm with pH was used for the determination of PMP pK_a's, shown Figure 6, and yielded two ionizations constants of 8.75 ± 0.08 (pyridine nitrogen) and 10.5 ± 0.4 (amino nitrogen) that are in good agreement with those determined previously (*43*).

(B) Labeled Protein. The UV/visible spectra of the native and freshly prepared aldolase−PMP complex showed a slight shift of the maximal absorbance to 329 nm (pH 6.0) compared to the PMP model compound (not shown). The absorbance changes at 329 nm that would accompany the deprotonation of pyridium and ammonium ions yield pK_a's of 6.9 ± 0.1 and 8.3 ± 0.5, respectively, and are shown in Figure 6. This represents an increase in acidity of ~2 pK units relative to the model compound and is not inconsistent with the presence of positively charged residues, such as Lys-146 that is adjacent to Lys-107. The proximity of two lysine residues in an active site has been shown to result in a pK_a decrease by several pK_a units (*44*). A lowered pK_a for Lys-107 would be mechanistically useful for nucleophilic attack on the carbonyl group of HNA-P during Schiff base formation.

Molecular Modeling of Aldolase−HNA-P Complexes. Molecular dynamics simulations were conducted to explore active site HNA-P configurations consistent with covalent complex formation as well as to gain insight into the exceptional stability of the covalent adduct formed by HNA-P and aldolase. Control simulations were first carried out in an effort to reduce computational overhead. Simulations of 1 ns duration each were run, comparing conformations generated for the unbound aldolase tetramer and that of a single unbound aldolase subunit. RMS deviations of atomic coordinates generated in each frame were <1.5 Å (based on C_α atomic positions) in the simulations when compared with respect to the initial crystallographic model and were <1.6 Å when comparing coordinates generated in identical frames between each of the simulations. These deviations are comparable with those obtained in simulations described in the literature (*45*, *46*) and warranted use of a single subunit in the molecular modeling of aldolase−HNA-P complexes.

(A) Noncovalent Aldolase−HNA-P Complex. Energy minimization yielded a stable HNA-P Michaelis complex, free of close contacts, filling the entire active site cleft and necessitated the expulsion of several water molecules in the crystal structure due to steric conflict. Simulation of 5 ns duration for phenol and phenate species showed the phosphate moiety to be persistently bound in its binding site. The oxyanion was anchored in its position by electrostatic interactions with Arg-303 and Lys-229 and by hydrogen bonds to backbone amides of Ser-271, Gly-272, Gly-302, and Arg-303 as well as with the Ser-271 side chain. Table 4 summarizes calculated distances and standard deviations of all oxyanion contacts made with active site residues.

In contrast, the orientations sampled for the naphthaldehyde moiety of HNA-P differed between the simulations for the phenol and phenate species. Torsional rotations in ω_1 and ω_2 resulted in the O_1 oxygen substituent for the naphthaldehyde moiety of HNA-P pointing in opposing directions that were approximately perpendicular with respect to its starting position within 200 ps of simulation. The ensemble of conformations sampled by the naphthaldehyde moiety resulted in few persistent hydrogen-bonding or electrostatic contacts with active site residues for the phenol species. Guanidinium moieties of Arg-42 and Arg-303, situated on opposite side of the naphthaldehyde moiety, participated in stacking interactions. The O_1 hydroxyl interacted with either Ser-35, Arg-42, or Arg-148 side chains intermittently. The distance between the attacking Lys-107 Nz and aldehyde C_{11} carbon averaged over the entire simulation was 5.8 (±1.3) Å. In only 0.27% of all frames were the configurations of Lys-107 and aldehyde competent for attack, and the averaged distance and angle of attack were 3.48 (±0.06) Å and 36° (±8°), respectively. In these frames,

Table 4: Contacts Made by Active Site Residues with the HNA-P Phosphate Oxyanion in the Michaelis Complex

HNA-P species	active site residue[a]						
	Ser-271	Lys-229	Arg-303	Ser-271 NH	Gly-272 NH	Gly-302 NH	Arg-303 NH
phenol	2.7 (±0.11)	5.2 (±0.42)	3.0 (±0.13)	2.9 (±0.14)	3.1 (±0.32)	2.8 (±0.12)	2.9 (±0.16)
phenate	2.9 (±0.15)	3.2 (±0.23)	2.9 (±0.12)	2.7 (±0.12)	3.6 (±0.85)	2.9 (±0.19)	2.8 (±0.12)

[a] Time-averaged distances and associated standard deviations, shown in parentheses, are in angstroms. Distances to backbone amides are indicated by the symbol NH.

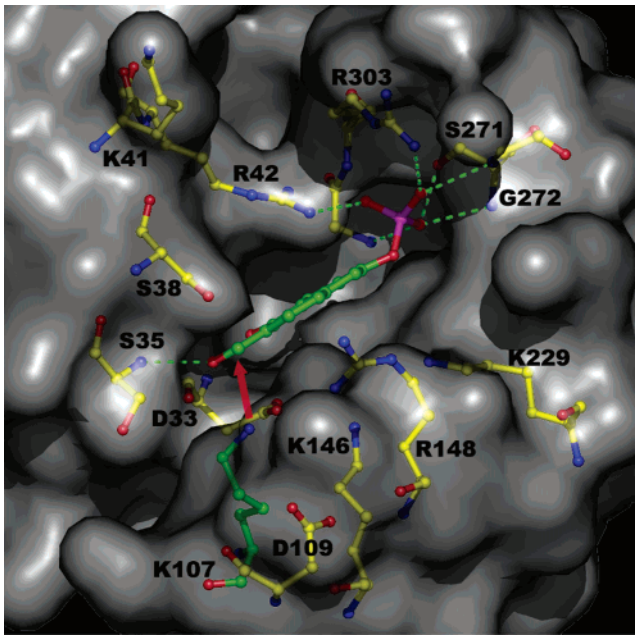

FIGURE 7: Frame generated by the simulation showing the Michaelis complex corresponding to the phenol species of HNA-P docked in the rabbit muscle aldolase active site cleft in a conformation competent for covalent bond formation. The solvent-accessible surface of the protein is depicted in gray. Dotted lines represent hydrogen bonds or electrostatic interactions, and active site residues proximal to HNA-P are labeled. The arrow shows the presumed trajectory corresponding to nucleophilic attack on the electrophilic C_{11} aldehyde carbon by Lys-107 Nz, the atom which is within close contact of the C_{11} carbon. The phosphate oxyanion of the HNA-P inhibitor is bound at the C_1-phosphate binding locus through hydrogen-bonding interactions with Lys-229, Ser-271, and Arg-303 as well as backbone amides that are maintained throughout the simulations. Guanidinium moieties of Arg-42 and Arg-303, situated on the opposite side of the naphthaldehyde moiety, make stacking interactions. The aldehyde O_{11} oxygen makes a hydrogen bond with Ser-35 NH in all frames competent for nucleophilic attack. Lys-146 is protonated and, although capable, does not hydrogen bond to the Lys-107 Nz nucleophile. The drawing was made with the program PyMOL (*48*).

the aldehyde O_{11} oxygen made a hydrogen bond with Ser-35 NH, 2.92 (±0.16) Å. The electrostatic interaction between the positive partial charges of the Lys-107 Nz hydrogens and negative partial charge of the aldehyde O_{11} oxygen influences the angle of attack and causes it to deviate from a value of 0° that would correspond to direct perpendicular attack of the Lys-107 Nz atom on the hybridization plane containing the aldehyde C_{11} carbon, an example of which is shown in Figure 7.

A more stable configuration was observed for the phenate species due to additional persistent contacts made with active site residues and resulted in a shorter averaged distance between the attacking Lys-107 Nz and aldehyde C_{11} carbon of 5.0 (±1.1) Å. Stabilizing electrostatic interactions involved the phenate O_1 oxygen with Lys-146 and Arg-148 side chains, averaged distances of 3.03 (±0.3) Å and 2.95 (±0.3) Å, respectively. In 80% of the frames, the aldehyde O_{11} oxygen interacted with an active site residue that was either Glu-34 NH, Ser-35 NH, Ser-35 side chain, or Ser-38 side chain. Geometries consistent with potential attack that had an angle of attack <20° were observed in 0.14% of the frames, <30° in 0.73%, and <40° in 1.7% of the frames. However, in no instance was the aldehyde O_{11} oxygen within close contact of a residue capable of acting as a general acid in either species. Hydrogen bonding between Lys-107 and Lys-146 was not observed in geometries considered competent for attack. Distances between Lys-107 and Lys-146 were 6.5 (±0.1) Å and 7.3 (±1.1) Å for phenol and phenate species, respectively. Potential energies profiles for each species showed no trend with time and were statistically identical as the average energy difference between species was less than their respective standard deviations (~620 kJ/mol).

(B) Covalent Aldolase−HNA-P Complex. Formation of the covalent adduct necessitated a displacement of the HNA-P molecule toward Lys-107 for bond formation with the aldehyde and resulted in the HNA-P oxyanion no longer interacting with the DHAP P_1-phosphate binding locus as was used to model the HNA-P Michealis complex. Simulations of 5 ns duration for both phenol and phenate species yielded essentially similar configurations for the HNA-P moiety in the active site. For each species, the HNA-P adduct adopted a similar ensemble of conformations that was roughly perpendicular to the starting position attained during the equilibration and remained in this orientation for the duration of the simulation. The conformations adopted by HNA-P throughout the simulations differed somewhat from those of the noncovalent adduct in the active site. The HNA-P phosphate underwent a torsional rotation in ω_1 and ω_2 such that the oxyanion was consistently displaced by ~7 Å toward the active site surface with respect to the noncovalent adduct (shown in Figure 7). Simultaneously, the HNA-P naphthaldehyde moiety underwent a rotational displacement within the active site cleft, pivoting by ~30° about the O_1 position for covalent bond formation with Lys-107 and leaving the naphthaldehyde moiety more solvent exposed in the covalent adduct.

To investigate the slow hydrolysis of the Schiff base, frames were analyzed as a function of water molecule accessibility with respect to the Schiff base formed and in particular hydrogen bonding by water molecules to Lys-107 Nz. A representative frame illustrated in Figure 8 shows the phenol species of the covalent adduct.

In both simulations, the phosphate oxyanion strongly interacted with Ser-38 and Lys-41, making hydrogen bonds in virtually all frames with averaged distances of 2.7 (±0.1) Å and 3.2 (±0.1) Å, respectively, for the phenol species and

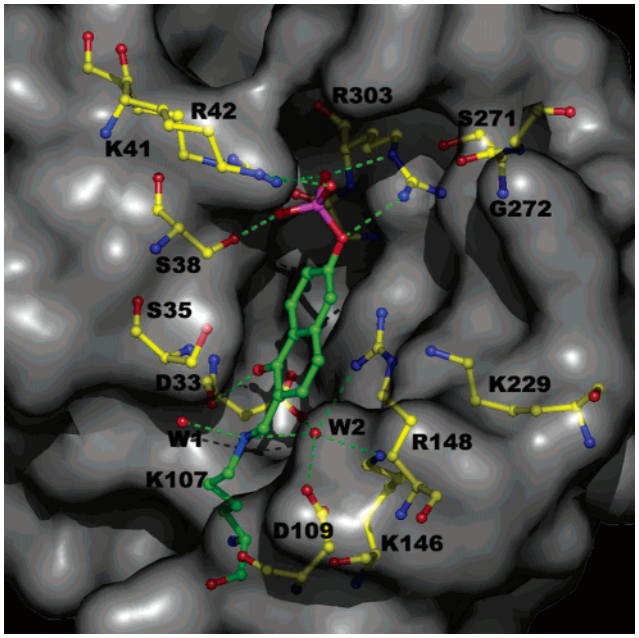

FIGURE 8: Snapshot from the dynamical simulation of the phenol species of the HNA-P covalent adduct formed with Lys-107 Nz of rabbit muscle aldolase. The solvent-accessible surface of the protein is depicted in gray. Dotted lines represent hydrogen bonds or electrostatic interactions, and active site residues are labeled. The orientation was chosen to maximize positional overlap of C_α atom positions of active site residues common to both figures. In all simulations, the phosphate oxyanion no longer binds the C_1-phosphate binding locus rather interacting with Ser-38 and Lys-41 and sometimes with Arg-303. Hydroxyl O_1 interacts with the Asp-33 backbone in the phenol species. In the majority of frames for phenol and phenate species, water molecules do not hydrogen bond to Lys-107 Nz (not shown). In simulations with phenol and phenate species where water molecules hydrogen bond Lys-107 Nz via the binding locus designated W_1, these water molecules do not interact with any amino acid capable of acting as a general base. For water molecules hydrogen bonding to Lys-107 Nz via the binding locus designated W_2, activation is possible by either Asp-33 or Asp-109; however, electrostatic attraction of the resulting hydroxyl ion with Lys-146 and/or Arg-148, which are within hydrogen-bonding distance of W_2, makes Schiff base hydrolysis unfavorable.

2.7 (±0.5) Å and 3.0 (±0.2) Å for the phenate species. Hydrogen bonding by the oxyanion to Arg-303 was observed only in a minority of frames (29.3% for the phenol and 42.7% for the phenate) and occasionally to Arg-42 (18.9% for the phenol and 0.7% for the phenate) and never simultaneously to both residues. In the case of the phenate species, interaction of Asp-33 with O_1 is repulsive compared to the phenol species, shown in Figure 8, where the interaction is attractive [averaged distance 2.8 (±0.2) Å]), and resulted in a slight displacement of the naphthalene ring to minimize O_1 interaction with Asp-33. Potential energy profiles for both species showed no trend with time and were considered statistically identical, the average energy difference between the two species being less than their respective standard deviations (610 kJ/mol). In both instances, the covalent adduct occluded the active site residues Lys-146 and Lys-229 throughout the entire simulation.

(C) Water Molecule Interaction. In the majority of the frames (64% for phenol and 62% for phenate species), no water molecules bound to Lys-107 Nz compared to a control surface residue Lys-321, whose Nz atom bound water molecules in all frames, indicating reduced solvent accessibility for Lys-107 Nz. Hydrogen bonding of water molecules with Lys-107 Nz, as shown in Figure 8, was observed in only a minority of the frames. Water molecule (W_2) hydrogen bonding to Asp-33, Asp-109, Lys-146, and occasionally Arg-148 as well as Lys-107 was observed in 23% of the frames for the phenol simulation and 27% of the frames in the case of the phenate. Hydrogen bonding to Lys-107 Nz by the W_1 water molecule also shown in Figure 8 was observed in 13% (phenol) and 11% (phenate) of the frames. Variation in the position of the W_1 binding site was qualitatively considerably larger than for W_2, which was essentially constant with respect to its interaction partners. Contrary to the W_2 molecule, the W_1 did not participate in any hydrogen bonds with amino acid side chains capable of acting as a general base. In only a minority of the frames (3% for phenol and 6% for phenate species) did two water molecules interact with Lys-107, as shown in Figure 8.

DISCUSSION

NA-P_2−Aldolase Interaction. Aromatic bisphosphorylated substrate analogues of fructose-1,6-bisphosphate aldolases strongly interact with the enzyme active site and represent compounds of considerable interest. The naphthalenic derivative NA-P_2 (K_i = 0.28 μM) represents one of the most potent competitive inhibitors for rabbit muscle aldolase-catalyzed reaction. Similar trends were noted using inhibitors of rat muscle aldolase also possessing aromatic moieties (*38*). The rigid structure imposed by the aromatic rings compared to a compound, which is not conformationally restricted such as hexanediol 1,6-bisphosphate (K_i = 25 μM) (*47*), would suggest that a smaller configurational entropy loss upon active site binding by the rigid aromatic compound, compared to the conformationally mobile analogue, may contribute for the observed affinity differences in aldolase−inhibitor complex formation (*48*, *49*).

Aldolase has two distinct binding sites for inorganic phosphate (*27*). From protection experiments, the higher affinity site corresponds to the C_1-phosphate binding site of Fru(1,6)P_2 while the second site, of lower binding energy, binds the C_6-phosphate and involves the participation of the Lys-107 residue to the binding (*25*). The fact that the mutation of Lys-107 to Met increases both K_m of the substrate Fru(1,6)P_2 and K_i of the inhibitor NA-P_2 argues in favor of the same binding site for the phosphate moiety of each compound and also the involvement of this lysine residue to binding. In the structure of rabbit muscle aldolase soaked with substrate, Lys-107 indeed interacts with the C_6-phosphate of Fru(1,6)P_2 (unpublished data). The above considerations are consistent with an inhibition scheme in class I aldolases where substitution of one of the phosphate groups of NA-P_2 by an aldehyde group results in Schiff base formation between Lys-107 and HNA-P. Enzyme inactivation by PLP through Schiff base formation at Lys-107 further corroborates our approach (*25*).

Aldolase Inhibition by HNA-P. Incubation of aldolase with HNA-P leads to a time-dependent inhibition resulting in complete activity loss that is only very slowly reversed. The inactivation kinetics correspond to slow-binding inhibition consisting of a fast preequilibrium association followed by a slow and reversible rearrangement at the active site that results in enzymatic inactivation (*21*, *22*). Although the

structural change in going from NA-P_2 to HNA-P provoked a decrease in active site affinity ($K_i = 125\ \mu M$ for the fast process), HNA-P represents to date the most potent slow-binding inhibitor for a class I aldolase having an overall inhibition constant K_i^* value of ~24 nM. This inhibition can be made irreversible upon treatment of HNA-P−enzyme complex with sodium borohydride, in agreement with an inhibition mechanism involving Schiff base formation with an active site lysine residue. Accessibility of the BH_4^- ion by the Lys-107 Nz atom is consistent with results from the dynamical simulations where the Lys-107 Nz atom is accessible to a water molecule, W_1.

Aldolase−HNA-P Interaction. The reactivity of HNA-P toward aldolase was characterized and quantified by UV/visible difference spectroscopy (*15*) using the HNA-P reaction with aminocaproic acid as a reference system. The kinetics of aldolase−HNA-P complex formation differs from that of the model system where in the presence of aldolase two distinct first-order kinetic processes were observed: a rapid phase consistent with a stoichiometry of one HNA-P reacted with a single aldolase subunit and a slower reaction that results in a stoichiometry of ~2 molecules of HNA-P bound per aldolase subunit. Analysis of ESI/MS data is entirely consistent with the presence of these two adducts. The faster process, associated with the larger differential absorbance change, results in enzyme inhibition, and incubation with hexitol-P_2, which protects against inhibition, abolishes the rapid phase. Kinetic parameters derived from the faster rate process describing the Schiff base formation are in good agreement with those obtained from enzymatic inhibition studies, and both Schiff base formation and inhibition are maximal when approximately one molecule of HNA-P has been covalently bound per aldolase subunit.

There are three lysine residues, 107, 146, and 229, located in the active site of aldolase that each could give rise to Schiff base formation. Site-directed mutagenesis of these amino acid residues to neutral isosteric amino acids, K107M, K146M and K229M, yielded mutant proteins that displayed not only diminished catalytic activity but also modified Schiff base formation kinetics. The most significant change in HNA-P interaction with aldolase arose from the mutation K107M where the fast phase corresponding to Schiff base formation was suppressed and enzyme inactivation did not occur. The identification of Lys-107 as the residue responsible for the Schiff base formation is consistent with the results obtained from the other mutants. The UV/visible difference spectra from the K229M mutant does not differ from spectra observed for the wild-type enzyme, thus eliminating Lys-229 as a candidate amino acid implicated in enzyme inhibition. Although inhibition kinetics for the point mutant K146M were reduced from the wild-type enzyme in terms of rate of Schiff base formation, the point mutation did not modify the ability of the mutant to form this complex. From the rabbit muscle aldolase crystal structure (*5*), Lys-146 is proximal to Lys-107 such that the decrease in Schiff base formation is consistent with a role by Lys-146 in the inhibition mechanism pathway.

Slow Inactivation. Enzymatic inactivation is 4000-fold more efficient compared to model compound formation. The HNA-P dissociation constant is micromolar, which is similar in value to dissociation constants of other monophosphorylated inhibitor compounds (*15*), suggesting that the rate of covalent bond formation may be at the origin for the slow-binding reaction. Schiff base formation with HNA-P requires that Lys-107 be present in sufficient concentration as a nucleophile. Electrostatic charge destabilization due to the presence of an adjacent positive charge has been reported as a mechanism for pK_a reduction of a lysine residue (*44*, *50*). In rabbit muscle aldolase, although Lys-107 is adjacent to Lys-146, each participate in hydrogen-bonding interactions with water molecules that would mitigate their electrostatic repulsion and reduce charge destabilization. Hence, the observed pK_a reduction for Lys-107 of only ~2 units, and Lys-146 neutralization by mutation to Met that diminishes only by 9-fold the rate of inactivation is consistent with the Lys-146 charge having a smaller destabilizing effect on the Lys-107 pK_a.

Other mechanisms of nucleophilic activation of Lys-107 cannot be ruled out as contributing factors. A pK_a of ~5 for the surface residue Asp-109 roughly matches that of Lys-107 (pK_a ~8) and would suggest that electrostatic interaction between Lys-107 and Asp-109 could favor proton transfer in a general base catalysis mechanism, thereby rendering Lys-107 nucleophilic and which would simultaneously diminish Asp-109 repulsion with the HNA-P aldehyde oxygen. The small overall reductions in k_{app}, shown in Table 3, for both D33N and D33S mutants tend to exclude Asp-33 as being implicated in activating Lys-107 for nucleophilic attack by a similar mechanism. At pH 7.6, concentration of the Lys-107 nucleophile appears to be sufficient for Schiff base formation not to be rate determining and thus would not explain slow inactivation.

The molecular dynamics simulations indicate a low concentration of HNA-P species competent for Schiff base formation with aldolase. The observed slow rate of aldolase inactivation is consistent with very infrequent occurrence of reaction geometries for both phenol and phenate species. Furthermore, carbinolamine formation depends on a general acid to facilitate protonation of the O_{11} oxygen, which in the phenol species can be performed via intramolecular proton transfer from the ortho C_1 hydroxyl, oriented cis to the reactive aldehyde. By contrast, no residue could be identified in the case of the phenate species that was within close contact distance and capable of general acid catalysis, making HNA-P inactivation due to the phenate species mechanistically unlikely. The additional stabilizing interactions made by the phenate species would then competitively inhibit binding of the phenol species and further decrease the rate of inactivation. A reduced rate of inactivation due to increased concentration of the incompetent phenate species at higher pH is not inconsistent with the slower inactivation observed in rabbit muscle aldolase for an *o*-hydroxybenzaldehyde phosphate analogue at alkaline pH (*16*).

The simulations clearly indicate that formation of the covalent bond between Lys-107 and HNA-P aldehyde requires a conformational rearrangement in the active site by HNA-P. The conformational rearrangement involves breaking all six hydrogen bonds and one electrostatic interaction with the phosphate oxyanion in the noncovalent adduct (see Table 4), thereby creating a significant kinetic barrier to covalent bond formation. Formation in the covalent complex of fewer interactions by the phosphate oxyanion, one hydrogen bond with Ser-38 and a single electrostatic interaction with Lys-41, results in a contribution to the overall

reaction that is energetically unfavorable. The increased solvent exposure by the aromatic naphthaldehyde moiety would further tend to increase the conformational barrier leading to covalent adduct formation.

Electrostatic destabilization, although advantageous as a mechanism for increasing the concentration of the attacking lysine nucleophile, would promote slow inactivation by heightening kinetic barriers in formation of protonated intermediates in the Schiff base reaction (*51*). Aldolase inactivation at pH 7.6 by HNA-P as well as by PLP through a Schiff base mechanism involves obligate formation of a protonated ketimine at Lys-107. The presence of an ionized Lys-146 amine vicinal to Lys-107 would tend to destabilize a protonated chemical species at Lys-107, increase the kinetic barrier to protonated ketamine formation, and consequently diminish the rate of Schiff base formation. Such a mechanism, although feasible, may be of less importance in the case of aldolase inactivation by HNA-P as Lys-146 neutralization only modestly decreases the inactivation rate and only a slight reduction in Lys-107 pK_a is observed, presumably because the lysine residues do not engage in hydrogen bond formation in the presence of HNA-P as seen in the simulations. The slow inactivation rate thus stems from a number of factors that cumulatively make covalent bond formation kinetically unfavorable, including competitive inhibition by the phenate species, infrequent occurrence of competent reaction geometries, a substantial conformational barrier to covalent adduct formation, and, to a lesser extent, destabilization of the protonated ketimine in the adduct.

Tight-Binding Reversible Inhibition. Very slow dissociation of the covalent complex implies significant complex stability, due to inhibition of Schiff base hydrolysis that renders covalent bond formation quasi-irreversible. In the majority of the configurations generated during the simulations, Schiff base hydrolysis would not be possible because no water molecules associated with the Lys-107 Nz atom in the covalent adduct. In those frames where water molecules were found within hydrogen-bonding distance of Lys-107, as shown in Figure 8, hydrolysis of the Schiff base is not mechanistically feasible. Either activation of the water molecule is not possible due to the absence of a conjugate base, as in the case of W_1, or, if activated, as in the case of W_2, the resultant electrostatic attraction by the OH^- ion with either protonated Lys-146 or Arg-148 or both would substantially reduce the frequency of attack on the Lys-107 ketimine. Furthermore, activation of W_2 would be even more unfavorable in the case of the phenate species due to the negative charge on O_1.

An alternate mode of attachment by the HNA-P phosphate at the substrate C_6-phosphate binding locus cannot be excluded and could give rise to the observed side reaction. Lys-41 and Lys-152 are surface residues that are within an ~15 Å radius of Lys-107, and if the HNA-P phosphate binds to the substrate C_6-phosphate binding locus, either residue could participate in Schiff base formation with the HNA-P aldehyde. The higher pK_a of these lysine residues and weaker affinity of the C_6-phosphate binding site are consistent with the observed slow secondary reaction that is not maximal at the inhibitor concentrations used to inactivate the enzyme. Disruption of the C_6-phosphate binding site by the point mutations D33N and D33S is not inconsistent with a reduced affinity of the secondary binding site and rendering the secondary side reaction unobservable at the inhibitor concentrations employed in the study.

Implications for Drug Design. The interaction of HNA-P with aldolase provides insights for the design of a new class of inhibitors for aldolase-catalyzed reactions. On the basis of our study, functional groups, including phosphate, aldehyde, and naphthol moieties, of the HNA-P molecule are important for tight binding and represent a blueprint for future inhibitor design. Phosphorylated inhibitors, whose phosphate moieties are able to recognize the aldolase C_1-phosphate binding site, represent a desirable design feature in a potential inhibition strategy. Interaction with the substrate C_1-phosphate binding locus in the native enzyme involves not only hydrogen bonding with Ser-271, which is conserved in all class I aldolases, but also hydrogen bonding with backbone atoms of other active site residues making for a phosphate binding site that could be exploited in all class I isoenzymes. However, the presence of the phosphate group remains problematic in drug design because of the poor ability by phosphate monoesters to penetrate cell membranes. These impediments could be circumvented by synthesizing a prodrug that would mask the phosphate charges using an protecting group that can be enzymatically converted into the active phosphate monoester form once the prodrug has been internalized (*52*, *53*).

ACKNOWLEDGMENT

We thank Christine Munger for skillful assistance in providing purified recombinant enzymes of both native and mutated aldolase.

REFERENCES

1. Meyerhof, O., Lohman, K., and Shuster, Ph. (1936) Uder die Aldolase, ein Kohlenstoff-verknupfendes Ferment, *Biochem. Z. 286*, 301−331.
2. Horecker, B. L., Tsolas, O., and Lai, C. Y. (1972) *Enzymes, 3rd Ed. 7*, 213−258.
3. Rutter, W. J. (1964) Evolution of aldolase, *Fed. Proc., Fed. Am. Soc. Exp. Biol. 23*, 1248−1257.
4. Rose, I. A., Warms, J. V., and Kuo, D. J. (1987) Concentration and partitioning of intermediates in the fructose bisphosphate aldolase reaction. Comparison of the muscle and liver enzymes, *J. Biol. Chem. 262*, 692−701.
5. Sygusch, J., Beaudry, D., and Allaire, M. (1987) Molecular architecture of rabbit skeletal muscle aldolase at 2.7-Å resolution, *Proc. Natl. Acad. Sci. U.S.A. 84*, 7846−7850.
6. Blom, N., and Sygusch, J. (1997) Product binding and role of the C-terminal region in class I D-fructose 1,6-bisphosphate aldolase, *Nat. Struct. Biol. 4*, 36−39.
7. Gamblin, S. J., Davies, G. J., Grimes, J. M., Jackson, R. M., Littlechild, J. A., and Watson, H. C. (1991) Activity and specificity of human aldolases, *J. Mol. Biol. 219*, 573−576.
8. Dalby, A. R., Tolan, D. R., and Littlechild, J. A. (2001) The structure of human liver fructose-1,6-bisphosphate aldolase, *Acta Crystallogr., Sect. D: Biol. Crystallogr. 57*, 1526−1533.
9. Hester, G., Brenner-Holzach, O., Rossi, F. A., Struck-Donatz, M., Winterhalter, K. H., Smith, J. D. G., and Piontek, K. (1991) The crystal structure of fructose-1,6-bisphosphate aldolase from *Drosophila melanogaster* at 2.5 Å resolution, *FEBS Lett. 292*, 237−242.
10. Kim, H., Certa, U., Dobeli, H., Jakob, P., and Hol, W. G. (1998) Crystal structure of fructose-1,6-bisphosphate aldolase from the human malaria parasite *Plasmodium falciparum*, *Biochemistry 37*, 4388−4396.
11. Chudzik, D. M., Michels, P. A., de Walque, S., and Hol, W. G. (2000) Structures of type 2 peroxisomal targeting signals in two trypanosomatid aldolases, *J. Mol. Biol. 300*, 697−707.

12. Gefflaut, T., Blonski, C., Périé, J., and Willson, M. (1995) Class I aldolases: substrate specificity, mechanism, inhibitors and structural aspects, *Prog. Biophys. Mol. Biol. 63*, 301−340.
13. Blonski, C., Gefflaut, T., and Périé, J. (1995) Effects of chirality and substituents at carbon 3 in dihydroxyacetone-phosphate analogues on their binding to rabbit muscle aldolase, *Bioorg. Med. Chem. 3*, 1247−1253.
14. Gefflaut, T., Blonski, C., and Périé, J. (1996) Slow reversible inhibitions of rabbit muscle aldolase with substrate analogues: synthesis, enzymatic kinetics and UV difference spectroscopy studies, *Bioorg. Med. Chem. 4*, 2043−2054.
15. Blonski, C., De Moissac, D., Périé, J., and Sygusch, J. (1997) Inhibition of rabbit muscle aldolase by phosphorylated aromatic compounds, *Biochem. J. 323*, 71−77.
16. Blonski, C., Gefflaut, T., and Périé, J. (1998) Kinetic and spectroscopic study of slow-binding inhibition processes in aldolase, *J. Phys. Org. Chem. 11*, 793−802.
17. Page, P., Blonski, C., and Périé, J. (1999) Origin of the slow-binding inhibition of aldolase by D-glycero-tetrulose 1-phosphate (D-erythrulose 1-phosphate) from the comparison with the isosteric phosphonate analogue, *Eur. J. Org. Chem. 1999*, 28533−2857.
18. Opperdoes, F. R. (1987) Compartmentation of carbohydrate metabolism in trypanosomes, *Annu. Rev. Microbiol. 41*, 127−151.
19. Verlinde, C. L. M. J., Hannaert, V., Blonski, C., Willson, M., Périé, J., Fothergill-Gilmore, L. A., Opperdoes, F. R., Gelb, M. H., Hol, W. G. J., and Michels, P. A. M. (2001) Glycolysis as a target for the design of new anti-trypanosome drugs, *Drug Resist. Updates 4*, 50−65.
20. Schartz, D., and Beitner, R. (2000) Detachment of the glycolytic enzymes, phosphofructokinase and aldolase, from cytoskeleton of melanoma cells, induced by local anesthetics, *Mol. Genet. Metab. 69*, 159−164.
21. Morrison, J. F., and Walsh, C. T. (1988) The behavior and significance of slow-binding enzyme inhibitors, *Adv. Enzymol. Relat. Areas Mol. Biol. 61*, 201−300.
22. Schloss, J. V. (1988) Significance of slow-binding enzyme inhibition and its relationship to reaction-intermediate analogues, *Acc. Chem. Res. 21*, 348−353.
23. Hartman, F. C., and Brown, J. P. (1976) Affinity labeling of a previously undetected essential lysyl residue in class I fructose bisphosphate aldolase, *J. Biol. Chem. 251*, 3057−3062.
24. Gupta, S., Hollenstein, R., Kochlar, S., and Christen, P. (1993) Paracatalytic self-inactivation of fructose-1,6-bisphosphate aldolase. Structure of the crosslink formed at the active site, *Eur. J. Biochem. 214*, 515−519.
25. Anai, M., Lai, C. Y., and Horecker, B. L. (1973) The pyridoxal phosphate-binding site of rabbit muscle aldolase, *Arch. Biochem. Biophys. 156*, 712−719.
26. Morris, A. J., and Tolan, D. R. (1994) Lysine-146 of rabbit muscle aldolase is essential for cleavage and condensation of the C3−C4 bond of fructose 1,6-bis(phosphate), *Biochemistry 33*, 12291−12297.
27. Ginsburg, A., and Mehler, A. H. (1966) Specific anion binding to fructose diphosphate aldolase from rabbit muscle, *Biochemistry 5*, 2623−2634.
28. Racker, E. (1947) Spectrophotometric measurement of hexokinase and phosphohexokinase activity, *J. Biol. Chem. 246*, 7041−7050.
29. Baranowski, T., and Niederland, T. R. J. (1949) Aldolase activity of myogen A, *J. Biol. Chem. 180*, 543−551.
30. Kawahara, K., and Tanford, C. (1966) The number of polypeptide chains in rabbit muscle aldolase, *Biochemistry 5*, 1578.
31. Segel, I. H. (1975) *Enzyme Kinetics: Behavior and Analysis of Steady-State and Rapid Equilibrium Enzyme Systems*, Willey-Interscience, New York.
32. Meloche, H. P. (1967) Bromopyruvate inactivation of 2-keto-3-deoxy-6-phosphogluconic aldolase. I. Kinetic evidence for active site specificity, *Biochemistry 6*, 2273−2280.
33. Berendsen, H. J. C., van der Spoel, D., and van Drunen, R. (1995) GROMACS: A message-passing parallel molecular dynamics implementation, *Phys. Commun. 91*, 43−56.
34. Hess, B., Bekker, H., Berendsen, H. J. C., and Fraaije, J. G. E. M. (1997) LINCS: A linear constraint solver for molecular simulations, *Comput. Chem. 18*, 1463−1472.
35. Essman, U., Perela, L., Berkowitz, M. L., Darden, T., Lee, H., and Pedersen, L. G. (1995) A smooth particle mesh Ewald method, *Chem. Phys. 103*, 8577−8592.
36. Morris, A. J., and Tolan, D. R. (1993) Site-directed mutagenesis identifies aspartate 33 as a previously unidentified critical residue in the catalytic mechanism of rabbit aldolase A, *J. Biol. Chem. 268*, 1095−1100.
37. Berthiaume, L., Tolan, D. R., and Sygusch, J. (1993) Differential usage of the carboxyl-terminal region among aldolase isozymes, *J. Biol. Chem. 268*, 10826−10835.
38. Suh, B., and Barker, R. (1971) Fluorescence studies of the binding of alkyl and aryl phosphates to rat muscle aldolase, *J. Biol. Chem. 246*, 7041−7050.
39. Metzler, C. M., Cahill, A., and Metzler, D. E. (1980) Equilibriums and absorption spectra of Schiff bases, *J. Am. Chem. Soc. 102*, 6075−6085.
40. Johnson, R. J., and Metzler, D. E. (1970) Analyzing spectra of vitamin B_6 derivatives, *Methods Enzymol. 18A*, 433−471.
41. Heinert, D., and Martell, A. E. (1963) Pyridoxine and pyridoxal analogs. VI. Electronic absorption spectra of Schiff bases, *J. Am. Chem. Soc. 85*, 183−185.
42. Burr, M., and Koshland, D. E., Jr. (1964) Use of "reporter groups" in structure−function studies of proteins, *Proc. Natl. Acad. Sci. U.S.A. 52*, 1017.
43. Williams, V. R., and Neilands, J. B. (1954) Apparent ionization constants, spectral properties and metal chelation of the cotransaminases and related compounds, *Arch. Biochem. Biophys. 53*, 56−70.
44. Highbarger, L. A., Gerlt, J. A., and Kenyon, G. L. (1996) Mechanism of the reaction catalyzed by acetoacetate decarboxylase. Importance of lysine 116 in determining the pK_a of active-site lysine 115, *Biochemistry 35*, 41−46.
45. Baaden, M., Meier, C., and Sansom, M. S. (2003) A molecular dynamics investigation of mono and dimeric states of the outer membrane enzyme OMPLA, *J. Mol. Biol. 331*, 177−189.
46. Sulpizi, M., Rothlisberger, U., and Carloni, P. (2003) Molecular dynamics studies of caspase-3, *Biophys J. 84*, 2207−2215.
47. Harman, F. C., and Barker, R. (1965) An exploration of the active site of aldolase using structural analogs of fructose diphosphate, *Biochemistry 4*, 1068−1075.
48. Dudley, H. W., Searle, M. S., Mackay, J. P., Gerhard, U., and Maplestone, R. (1993) Toward an estimation of binding constants in aqueous solution: Studies of associations of vancomycin group antibiotics, *Proc. Natl. Acad. Sci. U.S.A. 90*, 1172−1178.
49. Schirmer, R. H., Müller, J. G., and Krauth-Siegel, R. L. (1995) Disulfide-reductase inhibitors as chemotherapeutic agents: The design of drugs for trypanosomiasis and malaria, *Angew. Chem., Int. Ed. Engl. 34*, 141−154.
50. Schmidt, D. E., Jr., and Westheimer, F. H. (1971) p*K* of the lysine amino group at the active site of acetoacetate decarboxylase, *Biochemistry 10*, 1249−1253.
51. Maurady, A., Zdanov, A., de Moissac, D., Beaudry, D., and Sygusch, J. (2002) A conserved glutamate residue exhibits multifunctional catalytic roles in D-fructose-1,6-bisphosphate aldolases, *J. Biol. Chem. 277*, 9474−9483.
52. Périgaud, C., Gosselin, G., Lefebvre, I., Girardet, J.-L., Benzaria, S., Barber, I., and Imbach, J.-L. (1993) Synthesis and antitumor activity of a new class of pyrazolo[4,3-e]pyrrolo[1,2-a][1,4]-diazepinone analogs of pyrrolo[1,4]benzodiazepines, *Bioorg. Med. Chem. Lett. 3*, 2521−2526.
53. Farquhar, D., Khan, S., Srivasta, D. N., and Saunder, P. P. (1994) Synthesis and antitumor evaluation of bis[(pivaloyloxy)methyl] 2′-deoxy-5-fluorouridine 5′-monophosphate (FdUMP): a strategy to introduce nucleotides into cells, *J. Med. Chem. 37*, 3902−3909.

BI0477992